Low-Grazing Angle Propagation and Scattering Above the Sea Surface in the Presence of a Duct Jointly Solved by Boundary Integral Equations

Christophe Bourlier, Hongkun Li, and Nicolas Pinel

***Abstract*—For a two-dimensional problem and at microwave radar frequencies, this paper presents a method to compute the field scattered by a highly conducting (the impedance boundary condition is applied) rough sea surface in the presence of a duct having a linear-square refractive index profile below a medium of constant refractive index. In a previous paper, the corresponding Green's function, which allows us to solve the propagation problem, has been derived without considering the sea surface. Using the boundary integral equation (BIE) method, this paper solves jointly the scattering problem from the sea surface and the propagation problem by including this Green's function in the BIE. In addition, to efficiently solve the linear system obtained from the method of moments by discretizing the integral equations, the forward-backward method is applied, which allows us to consider very long rough surfaces.**

***Index Terms*—Ducting environments, electromagnetic scattering, integral equations, nonhomogeneous media, parabolic wave equation, propagation, sea surface electromagnetic scattering.**

I. Introduction

In the past decades, researchers in the areas of applied electromagnetics and underwater acoustics have developed rigorous and asymptotic models for mathematically describing wave propagation over rough surfaces, as well as the scattering of waves by such surfaces. These studies also investigated the combined effects of atmospheric conditions (ducting conditions) and surface roughness on the propagation and scattering problems. To solve this issue, two main methods are available in the literature: the well-known parabolic wave equation (PWE) method [1], and the boundary integral equation (BIE) method [2]–[4].

Under the conditions of predominant forward propagation and scattering, i.e., when the rough sea surface is gently undulating and the angles of propagation and scattering are grazing, the PWE approximation gives satisfactory results. For a complete review of this method, see the textbook of Levy [1] and the references therein. The great advantage of the PWE method is that it can deal with most real-life inhomogeneous environments. Its main drawback is the underlying paraxial approximation leading to an approximation of the propagator (that is, the Green's function).

By contrast, the BIE method, which is based on the Helmholtz wave equation, rigorously calculates all surface field interactions. If the Green's function is known in an appropriate (spatial or spectral) domain, an integral equation can be written for the induced currents on the rough surface. From these currents and Huygens' principle, which requires the appropriate propagator, the scattered field at a point above the surface can then be computed. The advantage of the BIE method is that it is a rigorous method, but its main drawback is that the Green's function (propagator) is known only for a small class of refractive index profiles [10], [15]. That is why, when the BIE method is applied [2], the propagator is usually derived under the PWE approximation. In [5]–[8], the BIE method is applied for the scattering from rough sea surfaces at grazing angles without ducting effects. In [9], an accelerated BIE scheme is proposed for propagation over the ocean surface.

For a half-space having a linear square refractive index profile ($n^2(z) = 1 - \varepsilon z$, with $0 < \varepsilon \ll 1$ and the height $z \geq 0$, meaning that the transmitter and receiver heights have $z \geq 0$ and $z' \geq 0$, respectively), Awadallah and Brown [3], [4] derived the corresponding Green function used to calculate the currents on a perfectly conducting rough surface from the BIE method. For practical applications, the condition $z \geq 0$ and $z' \geq 0$ is not met because it corresponds to an environment having a refractive index n lower than one, since $n^2(z) = 1 - \varepsilon z$ with $\varepsilon > 0$. Nevertheless, the numerical results presented in these papers are very interesting and showed that the BIE method is a good candidate to improve the scattering/propagation prediction above the sea surface in comparison to the PWE combined with the split-step Fourier (SSF) method.

In practice, the refractive index profile decreases with increasing height up to a given altitude, and eventually reaches a constant value. In [11], Bourlier *et al.* derived the corresponding Green function of such an environment. In the same spirit as Awadallah and Brown [3], [4], the purpose of this paper is to include this Green function in the BIE method to solve, without approximation, the problem of scattering from a highly conducting rough sea surface. In addition, to solve efficiently the

Manuscript received July 01, 2013; revised October 18, 2013; accepted November 20, 2014. Date of publication December 12, 2014; date of current version January 30, 2015. This work was supported in part by the French Ministry of the "Redressement Productif (Direction Générale de la Compétitivité, de l'Industrie et des Services)" and the French ministry of defense (DGA), in the framework of the PRORASEM project, in cooperation between ONERA, ALYOTECH and UNAN-IETR.

C. Bourlier and H. Li are with the IETR (Institut d'Electronique et de Télécommunications de Rennes) Laboratory, LUNAM Université, Université de Nantes, Polytech Nantes, 44306 Nantes Cedex 3, France (e-mail: christophe.bourlier@univ-nantes.fr).

N. Pinel is with Alyotech Technologies, Rennes Atalante Beaulieu, 35700 Rennes, France.

Color versions of one or more of the figures in this paper are available online at http://ieeexplore.ieee.org.

Digital Object Identifier 10.1109/TAP.2014.2379945

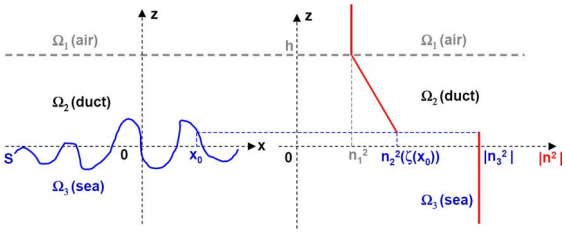

Fig. 1. On the left, illustration of the scattering problem. On the right, profile of the modulus of the square refractive index.

linear system obtained from the method of moments (MoM) by discretizing the integral equations, the forward-backward (FB) method is applied, which allows us to consider very long rough surfaces.

Section II briefly presents the integral equations and Green's function, and Section III presents the calculation of the incident field on the surface. Numerical results are presented in Section IV, and the last section gives concluding remarks.

II. Integral Equations and Green Function

Let us consider a two-dimensional space $\Omega = \Omega_1 \cup \Omega_2 \cup \Omega_3$ (see Fig. 1) made up of a homogeneous medium Ω_1 (defined for $z \geq h$) of constant refractive index n_1 over an inhomogeneous one Ω_2 (defined for $\xi \leq z < h$, duct), with a linear-square refractive index profile defined by $n^2(z) = n_1^2 + \varepsilon(h - z)$, with $\varepsilon > 0$, where $h > 0$ denotes the duct height. In addition, media Ω_2 and Ω_3 are separated by the rough sea surface. In media Ω_1 and Ω_2, the refractive indexes are positive real numbers, and the refractive index in Ω_3 is a constant complex number with a large imaginary part in comparison to one (i.e., highly conducting surface).

A. Integral Equations

The purpose of this article is to calculate the field scattered by the rough surface in medium Ω_2 when the source is located in medium Ω_2 by accounting for the refraction effect, since the medium Ω_2 is inhomogeneous. A method is needed to calculate the currents on the rough surface, then from the knowledge of these currents, to calculate the scattered field in Ω_2 from Huygens' principle.

Then, the currents on the surface S are computed from the BIE method that, in general, requires solving for both the field and its normal derivative. Since the sea surface is highly conductive for microwave frequencies, the impedance (or Leontovich) boundary condition (IBC) can be applied:

$$\begin{cases} \text{TE}: \quad \psi_2(\boldsymbol{r}) = \alpha_{\text{TE}} \frac{\partial \psi_2(\boldsymbol{r})}{\partial n} & , \alpha_{\text{TE}} = \frac{j}{k_0} \frac{n_{20}}{n_3} \\ \text{TM}: \quad \frac{\partial \psi_2(\boldsymbol{r})}{\partial n} = \alpha_{\text{TM}} \psi_2(\boldsymbol{r}) & , \alpha_{\text{TM}} = \frac{k_0}{j} \frac{n_{20}}{n_3} \end{cases}. \quad (1)$$

This leads to the following BIE [12], [13] for $\forall(\boldsymbol{r}, \boldsymbol{r}') \in S$

$$\begin{cases} \text{TE}: \psi_l(\boldsymbol{r}') = \int_S \frac{\partial \psi_2(\boldsymbol{r})}{\partial n} \left[g_2(\boldsymbol{r}, \boldsymbol{r}') - \alpha_{\text{TE}} \frac{\partial g_2(\boldsymbol{r}, \boldsymbol{r}')}{\partial n} \right] dS \\ \text{TM}: \psi_l(\boldsymbol{r}') = \frac{1}{2}\psi_2(\boldsymbol{r}') + \fint_S \psi_2(\boldsymbol{r}) \left[g_2(\boldsymbol{r}, \boldsymbol{r}') \alpha_{\text{TM}} - \frac{\partial g_2(\boldsymbol{r}, \boldsymbol{r}')}{\partial n} \right] dS \end{cases}. \quad (2)$$

In addition, n_3 (constant) is the refractive index of medium Ω_3, $n_{20} = \sqrt{n_1^2 + \varepsilon(h - \xi(x))} \approx \sqrt{n_1^2 + \varepsilon h}$ is the refractive index of medium Ω_2 for $\boldsymbol{r} \in S$, assumed to be independent of x, $k_0 = 2\pi/\lambda_0$ (λ_0 being the EM wavelength in free space) is the incident wave number of the source, which is assumed to be located inside Ω_2, ψ_l is the incident field on the surface, g_2 is the spatial Green's function in Ω_2 and $\boldsymbol{r} = x\hat{\boldsymbol{x}} + z\hat{\boldsymbol{z}}$ is a vector of components (x, z) in the Cartesian basis $(\hat{\boldsymbol{x}}, \hat{\boldsymbol{z}})$.

The surface current ($\psi_2(\boldsymbol{r})$ or $\partial\psi_2(\boldsymbol{r})/\partial n$) is computed by discretizing the integral equations from the MoM by using the point matching method with pulse basis functions. This leads to the linear system, $\bar{\boldsymbol{Z}}\boldsymbol{X} = \boldsymbol{b}$, where $\bar{\boldsymbol{Z}}$ the impedance matrix, $\boldsymbol{X}$ the unknown vector (of components $\partial\psi_2(\boldsymbol{r})/\partial n$ or $\psi_2(\boldsymbol{r})$ discretized on the surface) and $\boldsymbol{b}$ is the vector of components the incidence field discretized on the surface. If a direct LU inversion is applied to invert $\bar{\boldsymbol{Z}}$, the complexity is $\mathcal{O}(N^3)$, where N is the number of unknowns on the surface. To reduce this complexity to $\mathcal{O}(N^2)$, the Forward-Backward method [14] is applied, which allows us to consider long rough surfaces. In addition, the advantage of the FB is that only a row of the impedance matrix needs to be stored, instead of the whole matrix. The drawback is that the elements of the impedance matrix must be re-computed for each FB order.

The scattered field in Ω_2 is then computed by applying Huygens' principle, leading $\forall \boldsymbol{r} \in \Omega_2$ to

$$\psi_{\text{sca}}(\boldsymbol{r}) = \int_S \left[\psi_2(\boldsymbol{r}') \frac{g_2(\boldsymbol{r}', \boldsymbol{r})}{\partial n} - \frac{\partial \psi_2(\boldsymbol{r}')}{\partial n} g_2(\boldsymbol{r}', \boldsymbol{r}) \right] dS'. \quad (3)$$

Depending on polarization, $\psi_2(\boldsymbol{r})$ or $\partial\psi_2(\boldsymbol{r})/\partial n$ is known from the BIE solution; the companion quantity in (3) is again determined using the IBC in (1).

If Ω_2 is a homogeneous medium, then the spatial Green's function is well-known and is given by $g_2(\boldsymbol{r}, \boldsymbol{r}') = (j/4)\text{H}_0^{(1)}(k_0 \|\boldsymbol{r} - \boldsymbol{r}'\|) = g_{20}$, where $\text{H}_0^{(1)}$ is the zero-order Hankel function of the first kind. For an inhomogeneous medium, the spatial Green's function is more complicated, and is presented in the next subsection.

B. Spatial Green's Function

From [15]–[18], Bourlier *et al.* [11] evaluated the scalar Green's function for a homogeneous medium Ω_1 overlying a duct (medium Ω_2) with a linear-square refractive index profile (the rough surface was not considered). From the boundary conditions, the exact spectral Green's function is derived with the help of Airy functions. To have a closed-form expression of the corresponding spatial Green's function, the method of steepest descents (SD) is applied. The transmitter is located in either Ω_1 or Ω_2, and the receiver can also be located in either of these two regions, yielding four possible cases. In this paper, the most interesting case for practical applications is considered (receiver and transmitter within the duct Ω_2). For all $(\boldsymbol{r}, \boldsymbol{r}') \in \Omega_2$, the resulting spatial Green's function is then [11]

$$g_2(\boldsymbol{r}, \boldsymbol{r}') \approx \frac{e^{j\pi/4 + jk_0 R_{\text{PWE}}}}{2\sqrt{2\pi k_0 X}} \left[e^{j\phi_1} \frac{1 - s}{2} + A e^{j\phi_2} f(s\delta) s \right] \quad (4)$$

where

$$\begin{cases} R_{\mathrm{PWE}} = X + \frac{(z'-z)^2}{(2X)} \\ X = |x - x'| \\ \tau' = \sqrt{\varepsilon(h-z')} \\ \tau = \sqrt{\varepsilon(h-z)} \\ \phi_1 = -\frac{\varepsilon^2 X^3 k_0}{96} + \frac{\varepsilon X(2h-z'-z)k_0}{4} \\ \phi_2 = \frac{2k_0}{3\varepsilon}\left(\tau^3 + \tau'^3\right) - \frac{k_0(z'-z)^2}{2X} \\ \delta = \sqrt{\frac{k_0}{\varepsilon}}\sqrt{\frac{\tau\tau'}{\tau+\tau'}}\left(\frac{\varepsilon X}{2} - \tau - \tau'\right) \\ s = \mathrm{sgn}(\delta) \\ A = \sqrt{\frac{\varepsilon X}{2(\tau+\tau')}} \end{cases} . \tag{5}$$

In addition, the function f is defined as

$$f(\delta) = \frac{e^{-j\delta^2 - j\pi/4}}{\sqrt{\pi}} \int_{\delta}^{\infty} e^{ju^2} du = \frac{e^{-j\delta^2}}{2} \mathrm{erfc}\left(e^{-j\pi/4}\delta\right), \tag{6}$$

$$f(\delta) = \frac{j}{2\sqrt{\pi}\delta} + \frac{1}{4\sqrt{\pi}\delta^3} + \mathrm{o}\left(\frac{1}{\delta^3}\right) \quad \delta \gg 1 \tag{7}$$

and erfc is the complementary error function [19].

In (4), $\delta < 0$ ($s = \mathrm{sgn}(\delta) = -1$) corresponds to the illuminated region, for which the wave is propagating, whereas $\delta \geq 0$ ($s = \mathrm{sgn}(\delta) = +1$) corresponds to the shadow region, for which the wave is evanescent. For $\delta = 0$, $A = 1$, $\phi_1 = \phi_2$ and $f(\delta) = f(0) = 1/2$, so that (4) is continuous for $\delta = 0$. In the illuminated region $\delta < 0$, if $\varepsilon X \ll 2(\tau + \tau')$ and $|\delta| \gg 1$, then $A \ll 1$ and $|f(\delta)| \ll 1$, and the second term of (4) can be neglected. Then, the resulting equation corresponds to that obtained under the PWE given by

$$g_2(\boldsymbol{r}, \boldsymbol{r}') = \frac{e^{j\pi/4}}{2\sqrt{2\pi k_0 X}} \times e^{jk_0\left[X + (z'-z)^2/(2X) - \epsilon^2 X^3/96 + \epsilon X(2h-z-z')/4\right]}. \tag{8}$$

For X close to zero, the Green's function diverges (even when $z \neq z'$) because (4) has been derived under assumptions which are not valid for this case. This issue can be easily solved, somewhat heuristically, by noting that the refraction phenomenon can be neglected ($\varepsilon \approx 0$) for X close to 0 (more precisely, $R = \|\boldsymbol{r} - \boldsymbol{r}'\| = \sqrt{X^2 + (z'-z)^2}$ close to 0). Then, for $R \to 0$ and $\varepsilon \approx 0$, $g_2(\boldsymbol{r}, \boldsymbol{r}') \to (j/4)\mathrm{H}_0^{(1)}(k_0 \|\boldsymbol{r} - \boldsymbol{r}'\|) = g_{20}$, corresponding to Green's function of a homogeneous space of wavenumber k_0. In addition, for $k_0 R \gg 1$, $g_2(\boldsymbol{r}, \boldsymbol{r}') \approx e^{j\pi/4 + jk_0 R}/(2\sqrt{2\pi k_0 R})$, which is consistent with the first term of (4), since $\phi_1 \approx 0$, $s = -1$ (illuminated region), $R_{\mathrm{PWE}} \approx R$, and $X \approx R$ for the amplitude term. Then, (4) is transformed into

$$g_2(\boldsymbol{r}, \boldsymbol{r}') \approx \frac{j}{4}\mathrm{H}_0^{(1)}(k_0 \|\boldsymbol{r} - \boldsymbol{r}'\|) \underbrace{\left[e^{j\phi_1}\frac{1-s}{2} + Ae^{j\phi_2} f(s\delta)s\right]}_{\kappa(k_0, \boldsymbol{r}, \boldsymbol{r}')} \tag{9}$$

where the correction term κ due to the refraction has the property $\kappa \to 1$ when $R \to 0$. In the following, this equation is labeled as "Fock+NFC" because it was obtained from the textbook of Fock [17] with a near field correction (NFC), which is applied in this paper.

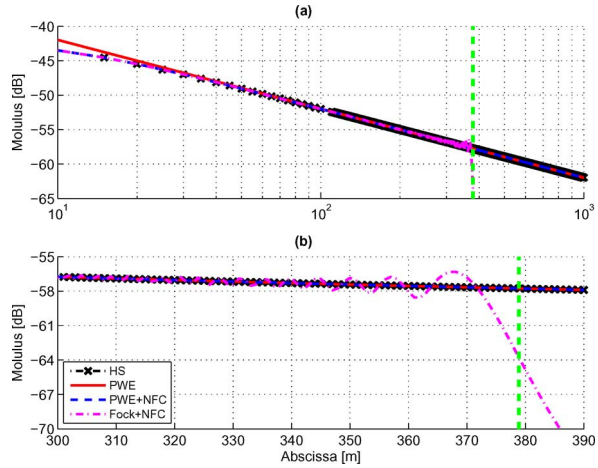

Fig. 2. Spatial Green's function g_2 versus the horizontal distance x in meters. (a) Modulus. (b) Zoom of (a) around X_0. The parameters are $x' = 0$ (transmitter abscissa), $z' = 10$ m (transmitter height), $z = 0$ m (receiver height) and see Table I for the values of λ_0 and h . The vertical dashed line indicates the separation between the illuminated and the shadow regions. (a). (b) Zoom.

TABLE I
SIMULATION PARAMETERS

Duct height h [m]	50
Duct parameter ε [m^{-1}]	5×10^{-3}
Wavelength λ_0 [m]	0.1 m
Sea permittivity ϵ_{r3}	$70.4 + 40.6j$
Surface length L [m]	600
Incidence angle θ_l [°]	88
Vertical footprint g_z [m]	2
Transmitter center $z_{a,0}$ [m]	10
Transmitter heights z_a [m]	$z_a \in [7; 13]$
Number of realizations N_r	70

The integral equations contain the normal derivative of the Green's function. The analytical expression for $\partial g_2(\boldsymbol{r}, \boldsymbol{r}')/\partial n$ is given in Appendix B.

Fig. 2(a) plots the spatial Green's function g_2 versus the horizontal distance X in meters and Fig. 2(b) zooms Fig. 2(a) around X_0. The vertical dashed line indicates the separation between the illuminated and shadow regions, for which the abscissa X_0 is defined by ($\delta = 0$ in (5))

$$X_0 = 2\left(\sqrt{\frac{h-z}{\varepsilon}} + \sqrt{\frac{h-z'}{\varepsilon}}\right). \tag{10}$$

The labels in the legend are:

- "HS," g_2 is computed by assuming that the medium Ω_2 is homogeneous ($g_2 = g_{20} = (j/4)\mathrm{H}_0^{(1)}(k_0 \|\boldsymbol{r} - \boldsymbol{r}'\|)$);
- "PWE," g_2 is computed from the PWE approximation, meaning $\forall X$ that $A = 0$ and $s = -1$ in (4);
- "PWE+NFC," g_2 is computed from the PWE approximation with a near-field correction, meaning that $g_2 = g_{20}e^{j\phi_1}$;
- "Fock+NFC," g_2 is computed from (9) (which includes near-field correction).

Near-field correction (NFC) means that the term $e^{j\pi/4 + jk_0 R_{\mathrm{PWE}}}/(2\sqrt{2\pi k_0 X})$ in (4) is replaced with g_{20} (the Taylor series expansion and the paraxial approximation $X \gg |z - z'|$ are not applied).

For X close to zero, Fig. 2 shows that the NFC corrects the modulus and, as expected, the NFC makes it possible to have good agreement with the results obtained by assuming a homogeneous space, since the refraction effect can be neglected when the receiver and the transmitter are very close. In the illuminated zone (on the left of the vertical dashed line), Fig. 2 shows that "Fock+NFC" and 'PWE+NFC" Green's functions match well and that the "Fock+NFC" function has an oscillatory behavior near the limit of the shadow zone because it is defined as the sum of two terms, leading to an interference phenomenon. In the shadow region, the "PWE+NFC" function decreases slowly, whereas the "Fock+NFC" 'function decreases rapidly. Then, the PWE approximation is not valid in this region.

III. Incident Field

The incident field, which appears in (2), is defined as the field produced by the source (antenna) that would exist in the duct in the absence of the rough surface. When the BIE/FB approach is used to simulate the problem of propagation over a rough surface in a ducting medium, it is appropriate to calculate the field produced by the source, the initial field, on a given vertical plane defined at $x = 0$. The incident field on the rough surface, is then evaluated by propagating the initial field from the vertical plane onto the rough surface using the ducting medium propagator. We use an initial field constructed from an angular spectrum of plane waves of the form [20]

$$\psi_l^a(z_a) = \frac{1}{\sqrt{\pi}\Delta\theta}\int_{-\pi/2}^{+\pi/2} e^{-(\theta-\theta_l)^2/(\Delta\theta)^2} e^{jk_0(z_a-z_{a,0})\cos\theta} d\theta \tag{11}$$

with

- θ_l the look angle measured from the positive z-axis;
- $\psi_l^a(z_a)$ the incident field on the surface S_a (z_a varies);
- $z_{a,0}$ the center of the antenna (constant number) with respect to z (the abscissa of the antenna is set to zero);
- $\Delta\theta = 2/(k_0 G) = 2/(k_0 g_z \sin\theta_l)$, in which G is the transverse width of the beam (perpendicular to the propagation axis) and g_z the vertical footprint (in the plane $x = 0$).

If the integration in (11) is performed in an exact manner, ψ_l^a satisfies the Helmholtz wave equation exactly. The field is therefore properly "Maxwellian." From Appendix A, the incident field on the rough surface S is then

$$\psi_l(\boldsymbol{r}) \propto \int_{S_a} \psi_l^a(\boldsymbol{r}_a) g_2(\boldsymbol{r}_a, \boldsymbol{r}) dS_a \tag{12}$$

where $\boldsymbol{r} = (x, \xi(x)) \in S$ and $\boldsymbol{r}_a = (0, z_a)$. The propagator $g_2(\boldsymbol{r}_a, \boldsymbol{r})$ is used because the transmitter is located in the duct. The computation of ψ_l requires two-fold numerical integrations. For very long surfaces, this computation is very time consuming. To solve this issue, first, an approximation of (11) is derived in Appendix C, which allows us to calculate ψ_l rapidly.

Fig. 3 plots the modulus of the incident field ψ_l^a on the surface S_a versus the height z_a in meters. The labels in the legend are:

- "Numerical," ψ_l^a is computed from a numerical integration ((11));
- "Analytical," ψ_l^a is computed analytically from (C5).

Fig. 3 shows a very good agreement between the results computed from a numerical integration and from the closed-form expression, validating the application of (C5), which has the advantage of not requiring a numerical integration.

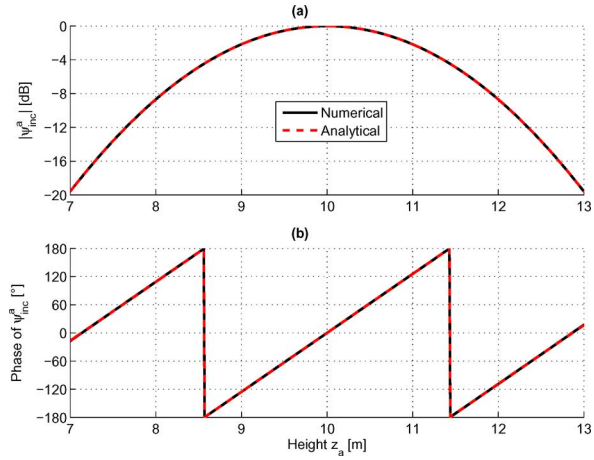

Fig. 3. Incident field ψ_l^a on the surface S_a versus the height z_a in meters. (a) Modulus. (b) Phase. The parameters are reported in Table I. The surface is assumed to be flat.

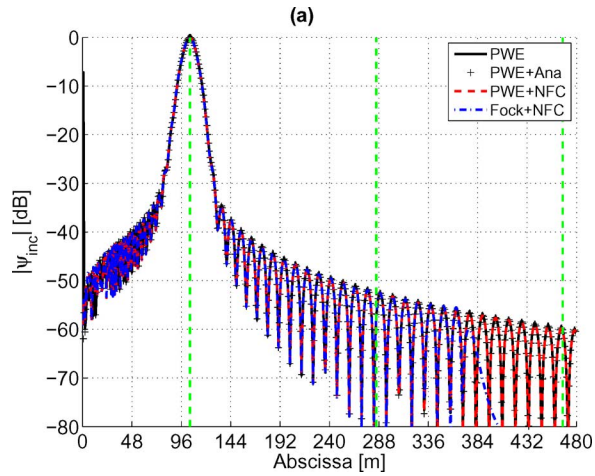

Fig. 4. Modulus of the normalized incident field ψ_l on the surface S versus its abscissa x in meters. The parameters are reported in Table I. The vertical dashed lines indicate the locations of the first, second, and third bounces.

Fig. 4 plots the modulus and the phase of the normalized incident field $\psi_l(\boldsymbol{r}')$ on the surface S versus its abscissa x in meters. The parameters are reported in Table I. The labels in the legend are:

- "PWE," ψ_l^a is computed from (11), and the PWE approximation is used for the calculation of the Green's function $g_2(\boldsymbol{r}_a, \boldsymbol{r})$ ((8));
- "PWE+Ana," ψ_l^a is computed from (C6) (no numerical integration), and the PWE approximation is used for the calculation of the Green's function $g_2(\boldsymbol{r}_a, \boldsymbol{r})$ ((8));
- "PWE+NFC," ψ_l^a is computed from (11), and the PWE approximation with near-field correction (NFC) is used for the calculation of the Green's function $g_2(\boldsymbol{r}_a, \boldsymbol{r}) = g_{20} e^{j\phi_1}$ in (12);
- "Fock+NFC," ψ_l^a is computed from (11), and (9) is used for the calculation of the Green's function.

Fig. 4 shows very good agreement between the results computed from "PWE" and "PWE+Ana," validating the application of (C6), which has the advantage of not requiring two-fold

numerical integrations. Fig. 4 also shows that the results computed from "PWE+NFC" and "PWE" match well, implying that the NFC is not required for propagation. This is due to the fact that the source is far from the zone of the illuminated surface. For $x = 0$, "PWE" predicts an overshoot because for $x = 0$, the Green's function is singular. Results computed from "Fock+NFC" and "PWE+NFC" match well in the illuminated zone and as expected, strongly differ in the shadow zone, over which "PWE+NFC" rapidly decreases. As a result, in the following, for "PWE" and 'PWE+NFC," (C6) will be used to compute ψ_l on the surface, whereas for "Fock+NFC," (9), (11) and (12) will be used.

In Fig. 4, the vertical dashed lines indicate the locations of the first, second and third bounces. They are obtained from a ray approach by calculating the ray trajectory. For more details, see Appendix D. As expected, the location of the maximum of $|\psi_l|$ coincides with the abscissa of the first bounce. In addition, the surface is large enough to observe the second and third bounces which will be predicted from the BIE/FB method in the next section. Fig. 4 also shows that the incident field on the edges of the surface is very small in comparison to the maximum. This avoids the edge diffraction phenomenon, which does not occur for practical applications. In addition, the length of the illuminated surface, for which the normalized field modulus is greater than -30 dB is 50 m, which is enough to include all the roughness scales of the sea surfaces considered.

IV. Numerical Results

The proposed method (BIE/FB) solves the scattering and propagation problems in three steps:

1) The field radiated by the transmitter (the antenna is modeled from (11)) is calculated on the sea surface from (12). It needs the knowledge of the Green's function, which depends on the profile of the refractive index. It is computed from (9).
2) The currents on the surface, ψ_2 and $\partial\psi_2/\partial n$, are computed by solving the boundary integral (2) (BIE). From the MoM, it is equivalent to solve a linear system. To decrease the memory requirement and the computing time, the forward–backward (FB) method is applied. This step uses the Green function of the first step, which shows that the propagation and scattering problems are correlated (in free space, the calculation of the currents is a scattering problem).
3) From the Huygens principle (3), the surface currents can radiate to give the scattered field measured by the receiver.

Simulation parameters are reported in Table I. For a perfectly conducting (PC) surface, $\epsilon_{r3} = j\infty$.

For the simulations, we consider that both the transmitter and the receiver are inside the duct. However, similar simulations for which either or both of them are outside the duct can be performed, since Green's function computed in [6] considered these cases.

A. Flat Surface

In this section, the surface is assumed to be flat and having the dielectric properties of sea water.

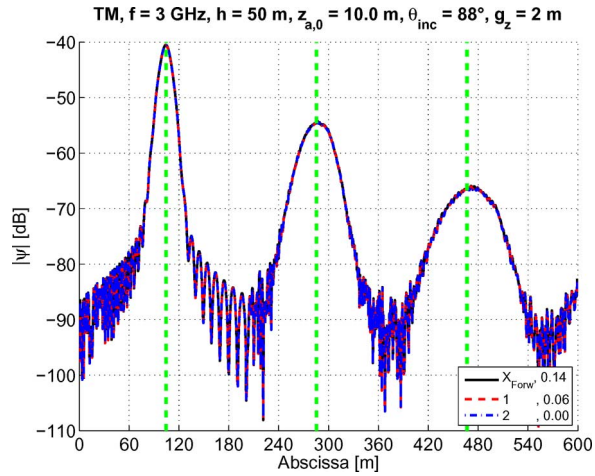

Fig. 5. Current modulus $|\psi_2|$ on a flat and IBC surface versus the surface abscissa x. The "Fock+NFC" Green's function is used and the polarization is TM. The vertical dashed lines indicate the locations of the first, second and third bounces.

Fig. 5 plots the current modulus $|\psi_2|$ on the surface versus the surface abscissa x. The "Fock+NFC" Green's function is used and the polarization is TM. The vertical dashed lines indicate the location of the first, second and third bounces (see Appendix D). In the legend, the first number corresponds to the iteration order of FB p_{FB}, starting from 1, and X_{Forw} is the current on the surface obtained for $p_{\mathrm{FB}} = 1$ by considering only the forward contribution (i.e., the backward contribution is not accounted for). The second number is a mean value defined by

$$\Delta_{\psi_2} = \frac{1}{N}\sum_{i=1}^{N} |20\log_{10}|\psi_{2,p_{\mathrm{FB}}} - \psi_{2,P_{\mathrm{FB}}}|| \qquad (13)$$

where $\psi_{2,p_{\mathrm{FB}}}$ is the surface current at the abscissa x and computed at the order p_{FB} and, $P_{\mathrm{FB}} = 3$ is the FB convergence order. It is obtained when the relative residual error (RRE) between two consecutive orders of the FB is smaller than 0.01. RRE is defined as $\mathrm{norm}(\boldsymbol{B}_{i+1} - \boldsymbol{B}_i)/\mathrm{norm}(\boldsymbol{B}_{i+1})$, in which $\boldsymbol{B}_i$ is the surface currents at the order i, and the symbol norm stands for the norm two (Euclidean norm).

As expected, due to the refraction effect, the current on the surface exhibits different locations for which the current modulus is maximum at an abscissa corresponding to those computed from a ray approach. The first spot (zone over x for which the current contributes) has a nearly Gaussian shape like the incident beam. Indeed, the first spot is strongly related to the incident field, which has a narrow beam centered on θ_l. As the abscissa x increases, the second spot still has a Gaussian shape, but the beam waist is larger than the first spot due to refraction. Awadallah and Brown [3], [4] also observed this behavior. Fig. 5 shows that the FB method converges rapidly and that the order of convergence is $P_{\mathrm{FB}} = 1$, since the results are very close to those obtained for $p_{\mathrm{FB}} = 1$ and $p_{\mathrm{FB}} = 2$. In addition, for $p_{\mathrm{FB}} = 1$, the backward contribution can be neglected.

Fig. 6 plots the total field modulus $|\psi_{\mathrm{sca}} + \psi_l|$ versus the abscissa x and the height z. The parameters are the same as in Fig. 5. Fig. 7 plots the same variations as in Fig. 6, but for three specific heights $z = z_0 = \{5, 10, 15\}$ m.

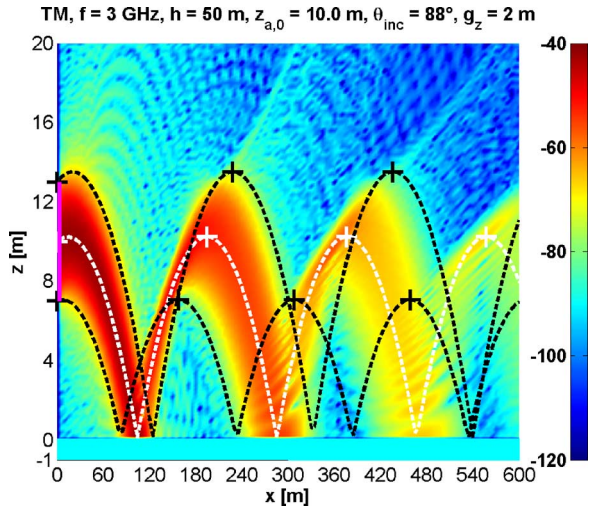

Fig. 6. Total field modulus $|\psi_{\rm sca}+\psi_l|$ versus the abscissa x and the height z. Same parameters as in Fig. 5. On the left, the pink vertical line indicates the source extent centered on $z_{a,0}$. The white dashed line plots the ray trajectory for a source located at $(0, z_{a,0})$ (indicated by a white cross). The black dashed line plots the ray trajectory for a source located at $(0, \max(z_a))$. The other crosses give the locations of the extrema (maximum heights of the ray trajectories, see Appendix D) of coordinates $(z_{\max,n}, x_{\max,n})$ (n is the number of bounces). The order $p_{\rm FB} = 2$.

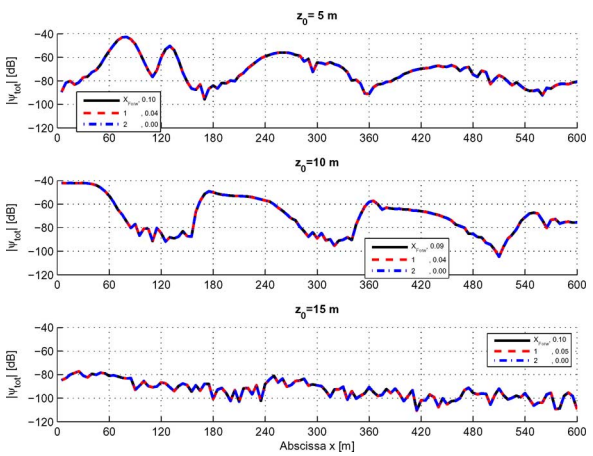

Fig. 7. Same variations as in Fig. 6, but for three specific heights $z = z_0$.

Fig. 6 shows that the results are consistent with those obtained from a ray approach. For $z > z_{\max,n} = 13.2$ m (by considering $\max(z_a)$ and n is the number of bounces), the total field decreases rapidly (see also Fig. 7). As x increases, the interference zone between the spots increases.

Fig. 8 plots the same variations as in Fig. 7, but for TE polarization and $p_{\rm FB} = \{3, 4\}$ instead of $p_{\rm FB} = \{1, 2\}$ in Fig. 7. In addition, the convergence order is $P_{\rm FB} = 5$ instead of $P_{\rm FB} = 3$. In comparison to the TM polarization, the FB order of convergence is greater, but the order $p_{\rm FB} = 1$ remains sufficient to have good accuracy, and the backward contribution can again be neglected.

Fig. 9 plots the same variations as in Fig. 5, but for both PC and IBC surfaces and $p_{\rm FB} = 1$. Fig. 10 plots the same variations as in Fig. 9, but for TE polarization. For TE polarization, the results obtained for PC and IBC surfaces match very well, meaning that the sea surface can be assumed to be PC. By contrast, for the TM polarization, the sea surface can not be considered as PC. This comes from the fact that for the TM (or V) polarization, the Fresnel reflection coefficient can be close to zero near the Brewster angle θ_B. For $\epsilon_{r3} = 70.4 + 40.6j$, $\theta_B \approx 83°$ which is close to the angle of the first bounce at the surface $\theta_{\rm inc,1} = \arccot(b_1) = \arccot(\sqrt{\cot^2\theta_l + \varepsilon z_a}) = 77.25°$ with $z_a = z_{a,0} = 10$ m.

Fig. 11 plots the same variations as in Fig. 5, but for "Fock+NFC," "PWE+NFC" and "PWE" Green's functions

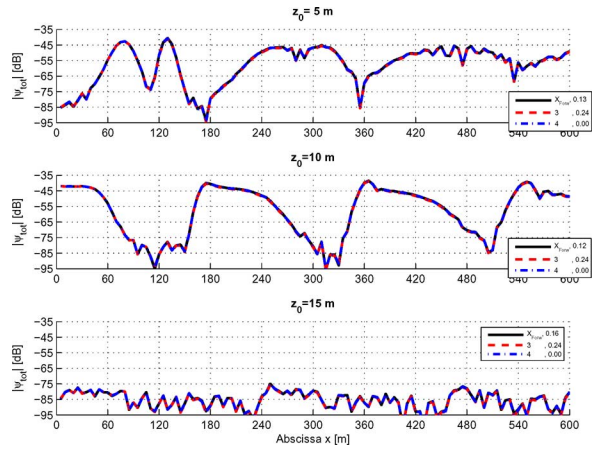

Fig. 8. Same variations as in Fig. 7, but for TE polarization.

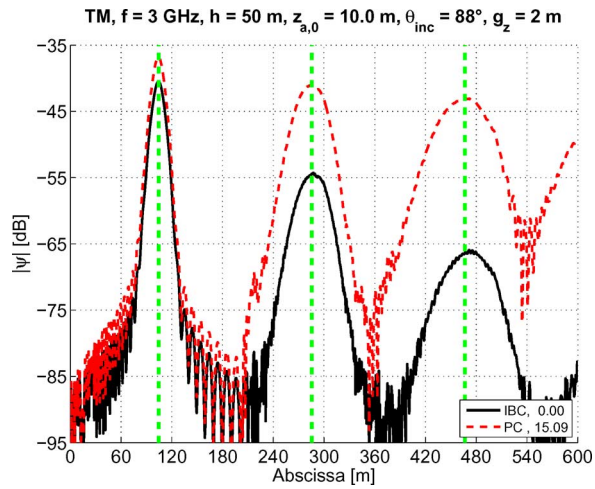

Fig. 9. Same variations as in Fig. 5, but for both PC and IBC surfaces and $p_{\rm FB} = 1$.

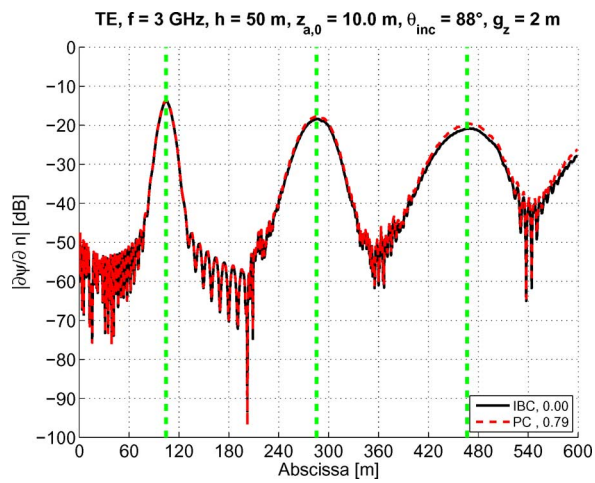

Fig. 10. Same variations as in Fig. 9, but for the TE polarization.

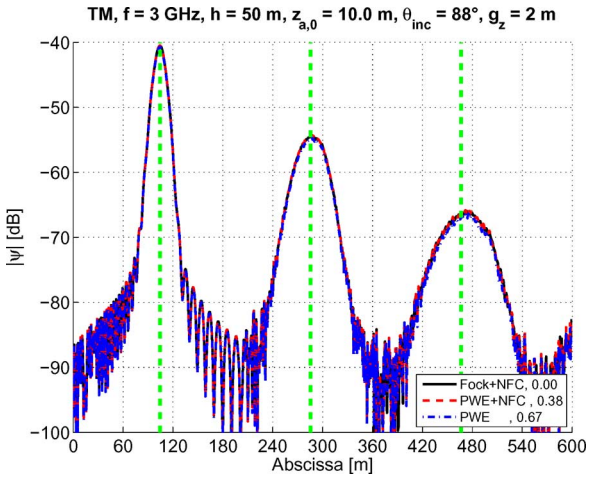

Fig. 11. Same variations as in Fig. 5, but for for "Fock+NFC,""PWE+NFC" and "PWE"Green's functions and $p_{\mathrm{FB}} = 1$.

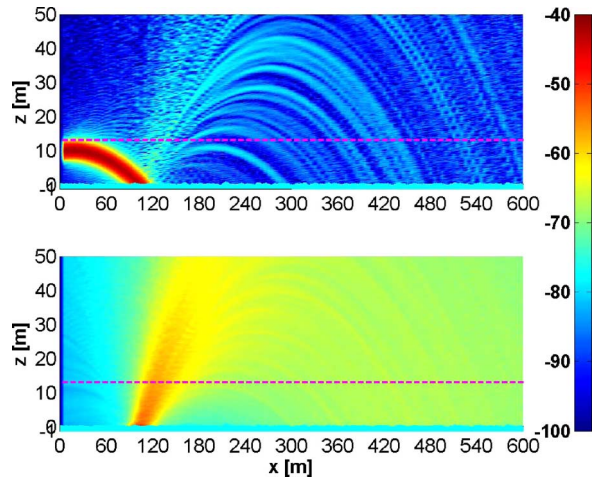

Fig. 12. Total scattered power versus the abscissa x and the height z. The simulation parameters are given in the caption of Fig. 3. Moreover, the wind speed is $u_{10} = 10$ m/s and the polarization is TM. (a) coherent component. (b) incoherent component. The horizontal dashed line indicates the maximum height $z_{\max,n} = 16.9$ m (maximum height of the ray trajectories).

and $p_{\mathrm{FB}} = 1$. For the PWE, the derivation of the diagonal elements of the impedance matrix is reported in Appendix E. Fig. 11 shows that the results computed from "Fock+NFC" and "PWE+NFC" match very well, meaning that the inclusion of the second term in (9) can be neglected and $s = -1$. This is equivalent to considering that the Green's function does not vanish in the shadow zone. Fig. 11 also shows that the results computed from "PWE+NFC" and "PWE" are in good agreement, except for x near 0 (transmitter abscissa), for which an overshoot appears (not shown here), because the Green's function is singular. This means that for $x \neq 0$ the near-field correction (NFC) has a small impact on the computation of the currents on the surface. By contrast, simulations not depicted here showed that the PWE cannot be applied for the computation of ψ_{sca}. This comes from the fact that the paraxial approximation ($|x - x'| \gg |z - z'|$) is not valid during the integration over x' of (3). Indeed, for a given x, during the integration over x', x' can be close to x, making the paraxial approximation invalid.

B. Random Rough Sea Surface

In this section, the roughness of the sea surface is taken into account. It is assumed that the rough surface height is a Gaussian stationary stochastic process with zero mean value, and that the height spectrum obeys the Elfouhaily *et al.* hydrodynamic spectrum [22], in which the key parameter is the wind speed u_{10} at 10 meters above the sea surface. The simulation parameters are reported in Table I.

The RMS surface heights σ_z corresponding to wind speeds $u_{10} = \{5, 10\}$ m/s, are $\sigma_z = \{0.161, 0.643\}$ m. For a given incidence angle $\theta_{\mathrm{inc},1}$, the electromagnetic surface roughness is characterized by the Rayleigh parameter, $R_a = k_0 \sigma_z \cos\theta_{\mathrm{inc},1}$; for $\theta_l = 88°$, the values are $R_a = \{2.229, 8.918\}$.

For wind speeds $u_{10} = \{5, 10\}$ m/s and for TM and TE polarizations, numerical results not shown here demonstrated that, as for a flat surface, the FB method converges at order one and the backward contribution can be neglected. From a geometrical point of view, this can be explained by the fact that the probability that the field specularly backscattered by the surface is very small at low grazing angles. Indeed, this probability is related to $\exp(-\tan^2\theta_{\mathrm{inc},1}/[2\sigma_s^2]) \approx 0$, in which σ_s^2 is the surface slope variance.

Several independent surfaces are generated as realizations of the Gaussian random process using the spectral method. For each surface numbered p, the field ψ_p and its normal derivative $\partial\psi_p/\partial n$ are calculated, and then from (3), the total scattered field $\Psi_p = \psi_l + \psi_{\mathrm{sca},p}$ is computed. The average coherent and incoherent scattered powers are then computed.

Fig. 12 plots the total scattered power versus the abscissa x and the height z. The simulation parameters are given in the caption of Fig. 3. Moreover, the wind speed is $u_{10} = 10$ m/s and the polarization is TM. Fig. 12(a)–(b) plot the coherent and incoherent components, respectively. The horizontal dashed line indicates the height $z_{\max,n} = 13.2$ m (maximum height of the ray trajectories for a flat surface with $\max(z_a) = 13$ m). In comparison to Fig. 6 (flat surface), due to the surface roughness, the scattered power is not negligible above $z_{\max,n}$, because the roughness modifies the local specular angles (which are random variables). As expected, for x defined before the first bounce, the incoherent component is negligible, whereas for this region, the coherent power is strong, corresponding to the incident field. As the number of bounces increases, the power is more diffuse. Indeed, the incident field of the first bounce (which can be obtained from the propagation of the currents of the previous bounce) is random, unlike the incident field illuminating the first bounce, which is deterministic. In general, outside the first bounce region, the levels of the incoherent power are larger than those of the coherent power.

Fig. 13 plots the same variations as in Fig. 12, but for three specific abscissas $x = x_0 = \{5, 220, 425\}$ m, and only the coherent component is shown. The abscissas are chosen such that $x_0 \approx \{5, x_{\max,1}, x_{\max,2}\}$ (in the subscript, the integer stands for the number of bounces), where $x_{\max,1}$ and $x_{\max,2}$ are the abscissa of the ray trajectories for which the heights are maxima (indicated by black crosses in Fig. 6, $\max(z_a) = 13$ m). The results obtained for a flat ($u_{10} = 0$ m/s) surface and for a surface of wind speed $u_{10} = 5$ m/s are also shown. Fig. 14 plots

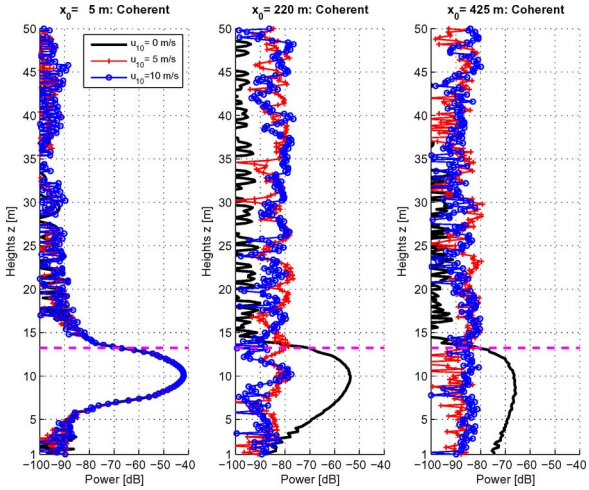

Fig. 13. Vertical cuts of the coherent power in Fig. 12 for different horizontal distances x_0 from the source. In addition to $u_{10} = 10$ m/s, the results for $u_{10} = 5$ m/s and $u_{10} = 0$ m/s (flat surface) are shown.

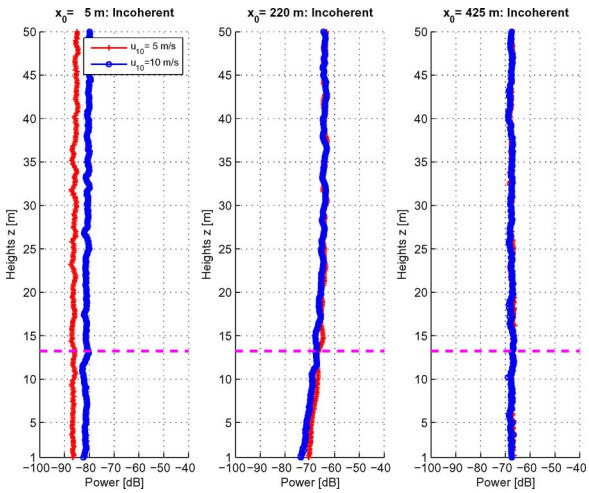

Fig. 14. Same variations as in Fig. 13, but for the incoherent component. For the flat surface case, the incoherent power is zero (minus infinity in dB scale) and is therefore not shown in the dB plots.

the same variations as in Fig. 13, but for the incoherent component. For $z < z_{\max,n}$, the coherent component is smaller than that obtained for a flat surface, whereas for $z > z_{\max,n}$, the opposite effect is observed. In addition, over this last region, the incoherent component remains nearly constant for $z < z_{\max,n}$. As for a flat surface, the interference phenomenon is strong, whereas for the incoherent component, this phenomenon is strongly damped. Awadallah and Brown [3], [4] also observed this behavior. As the height increases, Fig. 14 also shows that the incoherent component decreases as the wind speed decreases.

V. Conclusion and Discussion

In this paper, the propagation and scattering problems are solved jointly by solving numerically the BIE (scattering problem), in which the appropriate Green's function (propagation problem) is used to take into account refraction phenomena in the duct. To solve large problems, the BIE is combined with the FB method, which allows us to reduce the complexity to $\mathcal{O}(N^2)$ (N is the number of unknowns on the surface) and to store only one row of the impedance matrix at a time. The numerical results then showed that:

1) For the PWE, the near field-correction ("PWE+NFC") on the Green's function is necessary for the radiation of the currents, but it can be neglected for the current computation on the surface.
2) The shadowed region predicted by the propagator "Fock+NFC" can be omitted for both the calculation of the currents and of the fields radiated by the currents; this means that the propagator "PWE+NFC" is a very good approximation.
3) For TE polarization, the sea surface can be assumed to be perfectly conducting.
4) For TM polarization, the sea surface cannot be assumed to be perfectly conducting owing to the Brewster angle, and then the IBC approximation is applied.
5) The FB method converges very rapidly for a linear sea surface (no breaking waves), i.e., at the first order, and the backward contribution on the surface currents can be neglected.

In addition, the coherent and incoherent components of the the power scattered by a rough sea surface have been computed for wind speeds $u_{10} = \{5, 10\}$ m/s. The numerical results showed that, as the number of bounces increases, the coherent component shows strong fluctuations with respect to the observation height, whereas the incoherent power decreases monotonically with the observation height.

For the simulations, the duct parameter is $\varepsilon = 5 \times 10^{-3}$ m^{-1}. In practice, ε is of the order of 10^{-5} m^{-1}, meaning that to observe several bounces, the surface must be longer than that generated for $\varepsilon = 5 \times 10^{-3}$ m^{-1}. Nevertheless, the physical processes (scattering and propagation) remain nearly the same and then, the method proposed in this paper can be used as a benchmark method to validate asymptotic theories applied to calculate the propagation factor. See for instance [23] and the references therein. When the PWE is combined with the split-step Fourier (SSF) method, the boundary conditions (scattering problem) on the rough sea surface are determined from asymptotic models. It is important to note that, since the surface currents are computed from BIE, no approximation is used in this paper, except that the Green's function is derived from a saddle point technique [11].

In the future, to treat more realistic ducting environments, the Green function will be extended (from an analytical or a numerical way) to several layers having a linear square refractive index profile to investigate a tri-linear profile. This work is under investigation.

Appendix A
Approximation of the Incident Field

From the Huygens' principle, the incident field on the sea surface is determined by the field ψ_a on the aperture S_a and its normal derivative $\partial\psi_a/\partial n = \partial_n\psi_a$ as

$$\psi_l(\boldsymbol{r}) = \int_{S_a} \left[\partial_n g_2(\boldsymbol{r}_a, \boldsymbol{r})\psi_l^a(\boldsymbol{r}_a) - g_2(\boldsymbol{r}_a, \boldsymbol{r})\partial_n\psi_l^a(\boldsymbol{r}_a)\right] dS_a. \tag{A1}$$

Under the far-field approximation, the above equation can be simplified as

$$\begin{cases} \partial_n g_2(\boldsymbol{r}_a,\boldsymbol{r}) & \approx -jk_0 g_2(\boldsymbol{r}_a,\boldsymbol{r})\hat{\boldsymbol{R}}\cdot\boldsymbol{n}_a \\ \partial_n \psi_l^a(\boldsymbol{r}_a) & \approx +jk_0\psi_l^a(\boldsymbol{r}_a)\hat{\boldsymbol{r}}_a\cdot\boldsymbol{n}_a, \end{cases} \tag{A2}$$

where $\boldsymbol{n}_a$ is the unitary vector normal to the aperture, $\hat{\boldsymbol{R}}$ and $\hat{\boldsymbol{r}}_a$ are the unit vectors of $\boldsymbol{R}=\boldsymbol{r}-\boldsymbol{r}_a$ and $\boldsymbol{r}_a$, respectively. Then (A1) can be written as

$$\psi_l(\boldsymbol{r}) \approx -jk_0\int_{S_a}\psi_l^a(\boldsymbol{r}_a)g_2(\boldsymbol{r}_a,\boldsymbol{r})\left(\hat{\boldsymbol{R}}\cdot\boldsymbol{n}_a+\hat{\boldsymbol{r}}_a\cdot\boldsymbol{n}_a\right)dS_a. \tag{A3}$$

In addition, assuming that the field on the aperture S_a is locally plane, then $\hat{\boldsymbol{r}}_a\cdot\boldsymbol{n}_a=1$. If the propagation direction $\hat{\boldsymbol{R}}$ slightly deviates from $\boldsymbol{n}_a$ (case of grazing look angles), then $\hat{\boldsymbol{R}}\cdot\boldsymbol{n}_a\approx 1$. The incident field on the sea surface given by (A1) can then be approximated as

$$\psi_l(\boldsymbol{r}) \approx -2jk_0\int_{S_a}\psi_l^a(\boldsymbol{r}_a)g_2(\boldsymbol{r}_a,\boldsymbol{r})dS_a. \tag{A4}$$

Appendix B
Normal Derivative of the Spatial Green's Function

This Appendix presents the derivation of the normal derivative $\partial g_2(\boldsymbol{r},\boldsymbol{r}')/\partial n$ defined as

$$\frac{\partial g_2}{\partial n}=\boldsymbol{\nabla}g_2\cdot\hat{\boldsymbol{n}}=\frac{1}{\sqrt{1+\gamma^2}}\left(-\gamma\partial_x g_2+\partial_z g_2\right) \tag{B1}$$

where $\gamma = dz/dx$ is the surface slope, $\hat{\boldsymbol{n}} = (-\hat{\boldsymbol{x}}\gamma+\hat{\boldsymbol{z}})/\sqrt{1+\gamma^2}$ the normal to the surface pointing toward Ω_2, $\partial_x=\partial/\partial x$ and $\partial_z=\partial/\partial z$.

From (9), we have

$$\frac{\partial g_2}{\partial n}=\frac{\partial g_{20}}{\partial n}\kappa+g_{20}\frac{\partial\kappa}{\partial n} \tag{B2}$$

where

$$\begin{cases} g_{20}=\frac{j}{4}\mathrm{H}_0^{(1)}(k_0\left\|\boldsymbol{r}-\boldsymbol{r}'\right\|) \\ \frac{\partial g_{20}}{\partial n}=-\frac{jk_0}{4}\frac{\mathrm{H}_1^{(1)}(k_0\left\|\boldsymbol{r}-\boldsymbol{r}'\right\|)}{\left\|\boldsymbol{r}-\boldsymbol{r}'\right\|}\left(\boldsymbol{r}-\boldsymbol{r}'\right)\cdot\hat{\boldsymbol{n}} \end{cases}. \tag{B3}$$

In addition

$$\partial_x\kappa = j\partial_x\phi_1 e^{j\phi_1}\frac{1-s}{2}+Ae^{j\phi_2}f(s\delta)s \times\left[j\partial_x\phi_2+\frac{\partial_x A}{A}+s\partial_x\delta\left.\frac{\partial_x f(x)}{f(x)}\right|_{x=s\delta}\right] \tag{B4}$$

and $\partial_z\kappa$ is obtained from $\partial_x\kappa$ by substituting the subscript x for z.

Then, from (5), it can be shown that

$$\begin{cases} \partial_x\phi_1=-\frac{k_0\varepsilon^2X^2}{32}+\frac{k_0\varepsilon(2h-z'-z)}{4} \\ \partial_x\phi_2=\frac{k_0(z'-z)^2}{2X^2} \\ \frac{\partial_x A}{A}=\frac{1}{2X} \\ \partial_x\delta=\sqrt{\frac{k_0}{\varepsilon}}\sqrt{\frac{\tau\tau'}{\tau+\tau'}}\frac{\varepsilon}{2} \\ \partial_x f(x)=-2jxf(x)-\frac{e^{-j\pi/4}}{\sqrt{\pi}} \end{cases} \tag{B5}$$

and

$$\begin{cases} \partial_z\phi_1=-\frac{k_0\varepsilon X}{4} \\ \partial_z\phi_2=-k_0\tau-\frac{k_0(z-z')}{X} \\ \frac{\partial_z A}{A}=\frac{\varepsilon}{4\tau(\tau+\tau')} \\ \partial_z\delta=\sqrt{k_0\varepsilon}\left\{\frac{(2\tau+\tau')\sqrt{\tau'}}{4\sqrt{\tau+\tau'}\tau^{3/2}}-\frac{\varepsilon X}{8}\left[\frac{\tau'}{\tau(\tau+\tau')}\right]^{3/2}\right\} \\ \partial_z f(z)=-2jzf(z)-\frac{e^{-j\pi/4}}{\sqrt{\pi}} \end{cases}. \tag{B6}$$

Appendix C
Evaluation of the Incident Field on the Surface

This Appendix presents the evaluation of the incident field on the surface. First, a closed-form expression of (11) is found.

Using the approach of Toporkov *et al.* [21], setting $\theta=\theta_l+\delta$ and making a Taylor series expansion up to the second order over δ and around zero, we have

$$jk_0\left(z_a-z_{a,0}\right)\cos\theta \approx -a_0\delta^2+2bj\delta+c \tag{C1}$$

where

$$\begin{cases} a_0=\frac{c}{2} \\ b=\frac{k_0(z_a-z_{a,0})\sin\theta_l}{2} \\ c=jk_0\left(z_a-z_{a,0}\right)\cos\theta_l \end{cases}. \tag{C2}$$

The substitution of (C1) into (11) and the integration over δ lead then to

$$\psi_l^a(z_a)\approx\frac{1}{2\Delta\theta\sqrt{a}}e^{-(b^2/a)+c}\left\{\mathrm{erf}\left(\sqrt{a}\left[\frac{\pi}{2}-\theta_l\right]-\frac{jb}{\sqrt{a}}\right)+\mathrm{erf}\left(\sqrt{a}\left[\frac{\pi}{2}+\theta_l\right]+\frac{jb}{\sqrt{a}}\right)\right\} \tag{C3}$$

where $a=a_0+1/(\Delta\theta)^2$ and erf is the error function. From numerical trials, we showed that both erf functions give values very close to unity, leading to the following simplification:

$$\psi_l^a(z_a)\approx\frac{1}{\Delta\theta\sqrt{a}}e^{-(b^2/a)+c}. \tag{C4}$$

The term $e^c = e^{jk_0(z_a-z_{a,0})\cos\theta_l}$ gives the phase term and equals that of a plane wave. The term $e^{-b^2/a}$ is related to the damping of the wave.

For grazing angles $\theta_l\to\pi/2$, which implies that $1/(\Delta\theta)^2\gg a_0$ and then, $a\approx 1/(\Delta\theta)^2$. Equation (C4) becomes

$$\psi_l^a(z_a)\approx\exp\left(jk_0\left(z_a-z_{a,0}\right)\cos\theta_l-\frac{\left(z_a-z_{a,0}\right)^2}{g_z^2}\right). \tag{C5}$$

In [9] (Eq. (32)), this equation is used to calculate $\psi_l^a(z_a)$.

Using the Green's function under the PWE approximation given from (4), in which $s=1$ and $A=0$, we have from (C5) and (12) with $z_a\in[z_a^-;z_a^+]$ and $\boldsymbol{r}=(x,z)$

$$\psi_l(\boldsymbol{r})\approx A\int_{z_a^-}^{z_a^+}e^{-az_a^2+2bz_a+c}dz_a=\frac{A\sqrt{\pi}}{2\sqrt{a}}e^{(b^2/a)+c} \times\left[\mathrm{erf}\left(\sqrt{a}z_a^+-\frac{b}{\sqrt{a}}\right)-\mathrm{erf}\left(\sqrt{a}z_a^--\frac{b}{\sqrt{a}}\right)\right], \tag{C6}$$

where

$$\begin{cases} A = \frac{e^{j\pi/4}}{2\sqrt{2\pi k_0 x}}, \quad a = \frac{1}{g_z^2} - \frac{jk_0}{2x} \\ b = \frac{jk_0}{2}\left(\cos\theta_l - \cot\theta\right) + \frac{z_{a,0}}{g_z^2} \\ \cot\theta = \frac{\varepsilon x}{4} + \frac{z}{x} \\ c = jk_0\left[x + \frac{z^2}{2x} - \frac{\varepsilon^2 x^3}{96} + \frac{\varepsilon(2h-z)x}{4}\right] \\ \qquad -jk_0 z_{a,0}\cos\theta_l - \frac{z_{a,0}^2}{g_z^2} \end{cases}. \tag{C7}$$

Appendix D
Equation of the Ray Trajectory

For a linear square refractive index profile, the equation of the ray trajectory is a parabola [1]. Then, in Ω_2, for $x \in [x_a; x_{b,1}]$ where $x_{b,1}$ is the abscissa of the first bounce, the equation of the ray trajectory can be written as

$$z_0(x) = -\frac{\varepsilon(x-x_a)^2}{4} + b_0(x-x_a) + c_0 \tag{D1}$$

where b_0 and c_0 must be determined. Since $z_0(x_a) = z_a$ and $dz_0/dx|_{x=x_a} = \cot\theta_l$, $c_0 = z_a$ and $b_0 = \cot\theta_l$. It can be then shown that $x_{b,1} = x_a + 2(\cot\theta_l + \sqrt{\cot^2\theta_l + \varepsilon z_a})/\varepsilon$.

For the second arch of the parabola ($x \in]x_{b,1}; x_{b,2}]$), the equation of the ray trajectory can be written as

$$z_1(x) = -\frac{\varepsilon(x-x_{b,1})^2}{4} + b_1(x-x_{b,1}) + c_1 \tag{D2}$$

where b_1 and c_1 must be determined. Since $z_1(x_{b,1}) = z_0(x_{b,1}) = 0$ and $z_1'(x_{b,1}) = -z_0'(x_{b,1})$, we have $c_1 = 0$ and $b_1 = \sqrt{\cot^2\theta_l + \varepsilon z_a}$. The distance between two consecutive bounces is $d = x_{b,2} - x_{b,1} = 4b_1/\varepsilon$ and the coordinates of the extrema of the parabola is $(x_{b,1} + d/2, b_1^2/\varepsilon)$.

For the nth arch of the parabola ($x \in]x_{b,n}; x_{b,n+1}]$) ($n > 0$), the equation of the ray trajectory is then

$$z_n(x) = -\frac{\varepsilon(x-x_{b,n})^2}{4} + b_1(x-x_{b,n}) \tag{D3}$$

where $x_{b,n+1} = x_{b,n} + d$. The n points giving the maximum heights have coordinates ($x_{\max,n} = x_{b,n} + d/2, z_{\max,n} = z_a + \cot^2\theta_l/\varepsilon$).

Appendix E
Diagonal Elements of the Impedance Matrix Under the PWE Approximation

This Appendix presents the derivation of the elements of the impedance matrix under the PWE approximation with no NFC. The corresponding spatial Green's function is

$$g_2(\boldsymbol{r},\boldsymbol{r}') = \frac{e^{j\pi/4}}{2\sqrt{2\pi k_0 X}} \times e^{jk_0\left[X + (z'-z)^2/(2X) - \epsilon^2 X^3/96 + \epsilon X(2h-z-z')/4\right]}. \tag{E1}$$

For the diagonal elements, corresponding to $\boldsymbol{r} = \boldsymbol{r}'$, the refraction effect can be neglected, which is equivalent to take $\varepsilon = 0$ in the above equation. Then (the subscript 0 is added for $\varepsilon = 0$)

$$\begin{cases} \partial_x g_{20} = g_{20}\left[jk_0 - \frac{1}{2X} - \frac{jk_0(z'-z)^2}{X^2}\right] \\ \partial_z g_{20} = g_{20}\frac{jk_0|z-z'|}{X} \end{cases}. \tag{E2}$$

In general, from the point matching method, the diagonal elements D are derived from solving the following integral

$$D = \int_{x'}^{x'+\Delta} f(\boldsymbol{r},\boldsymbol{r}')dx \tag{E3}$$

where $f = g_2$ for the Dirichlet boundary conditions and $f = \partial g_2/\partial n$ for the Neumann boundary conditions, with $x \neq x'$ because for $x = x'$, $D = 1/2$, corresponding to $\psi_2/2$ in (2). In addition, Δ is the surface spatial sampling step.

For x close to x', $z' \approx z + \gamma'(x'-x)$, where $\gamma' = dz'/dx'$. Then, substituting this equation and (E1) (with $\varepsilon = 0$), (E2) into (E3), we can show that

$$D_{\mathrm{Dir}} = \frac{1}{k_0\sqrt{\pi(2+\gamma'^2)}}\int_0^{u_0} e^{ju^2}du \tag{E4}$$

and

$$D_{\mathrm{Neu}} = \frac{\gamma'}{4\sqrt{\pi(2+\gamma'^2)}}\int_0^{u_0} e^{ju^2}\left(2j\gamma'^2 + \frac{2+\gamma'^2}{u^2}\right)du \tag{E5}$$

for the Dirichlet and Neumann boundary conditions, respectively. In addition, $u_0 = \sqrt{k_0\Delta(2+\gamma'^2)}/\sqrt{2}$. Then,

$$D_{\mathrm{Dir}} = \frac{1}{k_0\sqrt{2(2+\gamma'^2)}}\mathrm{E}_1(u_0) \tag{E6}$$

and

$$D_{\mathrm{Neu}} = \frac{j\gamma'(1+\gamma'^2)}{\sqrt{2(2+\gamma'^2)}}\mathrm{E}_1(u_0) - \frac{\gamma'\sqrt{2+\gamma'^2}}{4\sqrt{\pi}}\frac{e^{ju_0^2}}{u_0} \tag{E7}$$

where

$$\mathrm{E}_1(u) = \mathrm{C}_1(u) + j\mathrm{S}_1(u) = \sqrt{\frac{2}{\pi}}\int_0^u e^{jt^2}dt \tag{E8}$$

in which C_1 and S_1 are the Fresnel integrals.

Acknowledgment

The authors would like to thank the reviewers for their careful reading of the manuscript as well as for providing many useful comments and suggestions on how to improve its content. Thanks also to Prof. J. T. Johnson for a careful reading.

References

[1] M. Levy, *Parabolic Equation Methods for Electromagnetic Wave Propagation*. London, U.K.: The Institution of Electrical Engineers, 2000, vol. 45, Electromagnetic Waves series.

[2] B. J. Uscinski, "Sound propagation with a linear sound-speed profile over a rough surface," *J. Acoust. Soc. Am.*, vol. 94, no. 1, pp. 491–498, 1993.

[3] R. S. Awadallah, "Rough Surface Scattering and Propagation over Rough Terrain in Ducting Environments," Ph.D., Virginia Polytech. Inst. State Univ., Blacksburg, VA, USA, 1998.

[4] R. S. Awadallah and G. S. Brown, "Low-grazing angle scattering from rough surfaces in a duct formed by a linear-square refractive index profile," *IEEE Trans. Antennas Propag.*, vol. 48, no. 5, pp. 1461–1474, May 2000.

[5] B. U. Ungan and J. T. Johnson, "Time statistics of propagation over the ocean surface: A numerical study," *IEEE Trans. Goesci. Remote Sens.*, vol. 38, no. 4, pp. 1626–34, Jul. 2000.

[6] D. E. Freund, N. E. Woods, H. -C. Ku, and R. S. Awadallah, "Forward radar propagation over a rough sea surface: A numerical assessment of the Miller-Brown Approximation using a horizontally polarized 3-GHz line source," *IEEE Trans. Antennas Propag.*, vol. 54, no. 4, pp. 1192–1304, Apr. 2006.

[7] D. E. Freund, N. E. Woods, H. -C. Ku, and R. S. Awadallah, "The effects of shadowing on modelling forward radar propagation over a rough sea surface," *Waves Random Complex Media*, vol. 18, no. 3, pp. 387–408, 2008.
[8] T. S. Hristov, K. D. Anderson, and C. A. Friehe, "Scattering properties of the ocean surface: The Miller-Brown-Vegh model revisited," *IEEE Trans. Antennas Propag.*, vol. 56, no. 4, pp. 1103–1109, Apr. 2008.
[9] R. S. Awadallah, M. T. Lamar, and J. R. Kuttler, "An accelerated boundary integral equation scheme for propagation over the ocean surface," *Radio Sci.*, vol. 37, no. 5, pp. 8-1–8-15, 2002.
[10] A. J. Robins, "Exact solutions of the Helmholtz equation for plane wave propagation in a medium variable density and sound speed," *J. Acoust. Soc. Amer.*, vol. 93, no. 3, pp. 1347–1352, 1993.
[11] C. Bourlier and N. Pinel, "Spatial Green function of a constant medium overlying a duct with linear-square refractive index profile," *IEEE Trans. Antennas Propag.*, vol. 61, no. 6, pp. 3172–3181, Jun. 2013.
[12] F. Harrington, *Field Computation by Moment Methods*. Piscataway, NJ, USA: IEEE Press, 1993.
[13] L. Tsang, J. A. Kong, K.-H. Ding, and C. O. Ao, *Scattering of Electromagnetics Waves: Numerical Simulations*. New York, NY, USA: Wiley Interscience, 2001.
[14] D. Holliday, L. L. DeRaad Jr., and G. J. St-Cyr, "Forward-Backward: A new method for computing low-grazing angle scattering," *IEEE Trans. Antennas Propag.*, vol. 44, no. 1, pp. 1199–1206, Jan. 1995.
[15] L. M. Brekhovskikh, *Waves in Layered Media*, Second ed. New York, NY, USA: Academic, 1980.
[16] L. B. Felsen and N. Marcuvitz, *Radiation and Scattering Waves*. London, U.K.: Prentice-Hall, 1973.
[17] V. A. Fock, *Electromagnetic Diffraction and Propagation Problems*. Paris, France: Pergamon, 1965.
[18] A. Kukushkin, *Radio Wave Propagation in the Marine Boundary Layer*. New York, NY, USA: Wiley-VCH (British Library), 2004.
[19] M. Abramowitz and I. A. Stegun, *Handbook of Mathematical Functions*. New York, NY, USA: Dover, 1972.
[20] E. Thorsos, "The validity of the Kirchhoff approximation for rough surface scattering using a Gaussian roughness spectrum," *J. Acoust. Soc. Amer.*, vol. 83, no. 1, pp. 78–92, 1988.
[21] J. V. Toporkov, R. S. Awadallah, and G. S. Brown, "Issues related to the use of a Gaussian-like incident field for low-grazing-angle scattering," *J. Opt. Soc. Amer. A*, vol. 16, no. 1, pp. 176–187, 1999.
[22] T. Elfouhaily, B. Chapron, K. Katsaros, and D. Vandermark, "A unified directional spectrum for long and short wind-driven waves," *J. Geophys. Res.*, vol. 102, no. C7, pp. 781–796, 1997.
[23] V. Fabbro, C. Bourlier, and P. F. Combes, "Forward propagation modeling above Gaussian rough surfaces by the Parabolic Wave Equation: Introduction of the shadowing effect," *Progress Electromagn. Res.*, vol. 58, pp. 243–269, 2006.

Christophe Bourlier was born in La Flèche, France, on July 6, 1971. He received the M.S. degree in electronics from the University of Rennes, Rennes, France, in 1995 and the Ph.D. degree from the SEI (SystèmeÉlectronique et Informatique) Laboratory. Nantes, France, in 1999.

He is now with IETR (Institute of Electronics and Telecommunications of Rennes, France) Laboratory, Nantes, at Polytech Nantes (University of Nantes, France). He is a Researcher at the National Center for Scientific Research working on electromagnetic wave scattering from rough surfaces (ocean like-surfaces) and objects for microwaves and infrared remote sensing applications and Radar signatures. He is author of more than 180 journal articles and conference papers.

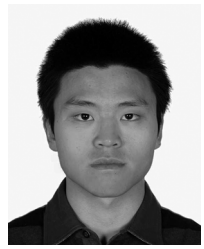

Hongkun Li was born in Guangdong, China, in July 1984. He received the B.S. and M.S. degrees in optics from the South China University of Technology, Guangzhou, China, in 2007 and 2010, respectively. and the M.S. and Ph.D. degrees in electronics from the University of Nantes, Nantes, France, in 2009 and 2012, respectively.

He is currently a Post-Doctoral Researcher with the IETR (Institute of Electronics and Telecommunications of Rennes, France) Laboratory at Polytech Nantes (University of Nantes, France). He works on infrared emission and reflection and microwave scattering problems concerning rough sea surfaces.

Nicolas Pinel was born in Saint-Brieuc, France, in 1980. He received the Engineering degree and M.S. degree in electronics and electrical engineering both from Polytech Nantes (Ecole Polytechnique de l'Université de Nantes), Nantes, France, in 2003 and the Ph.D. degree from the University of Nantes, France, in 2006.

He was with Polytech Nantes as a contractual Assistant Professor for two years, and then as a Research Engineer for five years. He has been an R&D Engineer at Alyotech, Rennes, France, since 2013. His research interests are in the areas of radar and optical remote sensing, scattering, and propagation. In particular, he works on asymptotic methods of electromagnetic wave scattering from random rough surfaces and layers.